nature physics

SUPPLEMENTARY INFORMATION

DOI: 10.1038/NPHYS4070

In the format provided by the authors and unedited.

Signatures of interaction-induced helical gaps in nanowire quantum point contacts

S. Heedt,[1,*] N. Traverso Ziani,[2] F. Crépin,[3] W. Prost,[4] St. Trellenkamp,[1] J. Schubert,[1] D. Grützmacher,[1] B. Trauzettel,[2] and Th. Schäpers[1,†]

[1]*Peter Grünberg Institut (PGI-9) and JARA-Fundamentals of Future Information Technology, Forschungszentrum Jülich, 52425 Jülich, Germany*
[2]*Institute of Theoretical Physics and Astrophysics, University of Würzburg, 97074 Würzburg, Germany*
[3]*Laboratoire de Physique Théorique de la Matière Condensée, UPMC, CNRS UMR 7600, Sorbonne Universités, 4 place Jussieu, 75252 Paris Cedex 05, France*
[4]*Solid State Electronics Department, University of Duisburg-Essen, 47057 Duisburg, Germany*

1. SPIN-ORBIT COUPLING IN THE NANOWIRE DEVICE

Weak Antilocalization Effect

The elastic mean free path of 250 nm[S1] is large for InAs nanowires but the contact separation is more than one order of magnitude larger. Hence, diffusive closed-loop electron trajectories give rise to the weak antilocalization effect in the open, unconfined regime. This is a strong indication for pronounced spin-orbit coupling. It is one of the most common techniques to quantify the relevance of spin-orbit coupling in mesoscopic semiconductors and involves conductance measurements in the phase-coherent transport regime. The signatures of the weak antilocalization effect reveal the presence of spin relaxation that results from spin-orbit coupling[S2–S4]. The nanowire conductance at $T = 50\,\mathrm{mK}$ and for a dc-bias voltage of $V_{\mathrm{dc}} = 50\,\mu\mathrm{V}$ is shown in Fig. S1. Here, 300 individual magnetoconductance sweeps have been averaged over the back-gate voltage interval from $-1.5\,\mathrm{V}$ to $1.5\,\mathrm{V}$ in order to average out magnetoconductance features that are not related to the weak (anti)localization correction to the conductance.
The quasiclassical model for the conductance correction that is employed to fit the data is given by[S5,S6]

$$\Delta G = -\frac{e^2}{h}\frac{1}{L}\left[3\left(\frac{1}{l_\varphi^2}+\frac{4}{3l_{\mathrm{so}}^2}+\frac{1}{l_B^2}\right)^{-\frac{1}{2}}-\left(\frac{1}{l_\varphi^2}+\frac{1}{l_B^2}\right)^{-\frac{1}{2}}\right.$$
$$\left.-3\left(\frac{1}{l_\varphi^2}+\frac{4}{3l_{\mathrm{so}}^2}+\frac{d}{l_e^2}+\frac{1}{l_B^2}\right)^{-\frac{1}{2}}+\left(\frac{1}{l_\varphi^2}+\frac{d}{l_e^2}+\frac{1}{l_B^2}\right)^{-\frac{1}{2}}\right], \tag{S1}$$

with the magnetic dephasing length

$$l_B = \sqrt{\frac{C_m}{d}\frac{l_m^4}{w^{\gamma_m} l_e^{2-\gamma_m}}} \tag{S2}$$

and the magnetic length $l_m = \sqrt{\hbar/eB}$. The dimensionality of the unconfined nanowire is $d = 3$ since the Fermi wavelength $\lambda_{\mathrm{F}} \approx 40\,\mathrm{nm}$ is smaller than the nanowire diameter ($w = 100\,\mathrm{nm}$). In the weak magnetic field limit, the magnetic dephasing (S2) has been quantitatively evaluated by Monte Carlo simulations of the quasiclassical trajectories in a hexagonal nanowire geometry by van Weperen *et al.*[S3]. If the magnetic field is aligned perpendicular to the nanowire axis, $C_m = 22.3 \pm 0.3$ and $\gamma_m = 3.174 \pm 0.003$. As depicted in Fig. S1 the fit yields an excellent agreement between the theoretical model and the experimental curve for a phase coherence length $l_\varphi = 670 \pm 98\,\mathrm{nm}$ and a spin relaxation length $l_{\mathrm{so}} = 546 \pm 48\,\mathrm{nm}$. Again invoking the Monte Carlo results by van Weperen *et al.*[S3], we can translate the spin relaxation length into a Rashba spin precession length L_{so} (which is defined in ref. S3 as a spin precession by 2 rad):

$$l_{\mathrm{so}} = \sqrt{\frac{C_s}{d}\frac{L_{\mathrm{so}}^4}{w^{\gamma_s} l_e^{2-\gamma_s}}}. \tag{S3}$$

Using the parameters $C_s = 8.7 \pm 0.5$ and $\gamma_s = 3.2 \pm 0.1$[S3] we obtain $L_{\mathrm{so}} = 121\,\mathrm{nm}$. Hence, $\alpha_{\mathrm{R}} = \hbar^2/m^* L_{\mathrm{so}} = 0.24\,\mathrm{eV\,Å}$ and $E_{\mathrm{so}} = m^*\alpha_{\mathrm{R}}^2/2\hbar^2 = 100\,\mu\mathrm{eV}$. This result is at the upper end of the spin-orbit coupling parameters found in the literature for InAs nanowires. It has to be kept in mind that this value corresponds to the back-gate voltage regime

around $V_{\mathrm{BG}} = 0\,\mathrm{V}$ and it has been shown that α_{R} can easily increase by a factor of about four upon application of a sizable potential gradient[S4,S7]. Such a substantial potential gradient occurs due to the application of a negative top-gate voltage V_{TG} related to the formation of the local quantum point contacts. Thus, the local top-gate voltage that is used to tune the subband occupation of the quantum point contact has profound impact on the Rashba-type spin-orbit coupling. This holds in particular at the first quantized conductance plateau close to the pinch-off of the 1D channel. The spin-orbit energy E_{so}, which is reflected in the location of the reentrant conductance feature on the G-V_{TG} curve, is actually augmented by the strong electric field of the local gate and the additional contribution from the back gate.

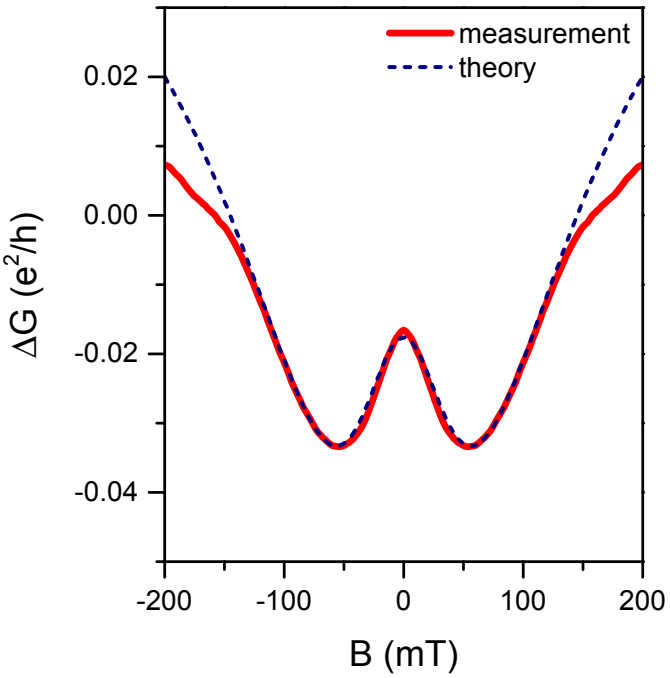

FIG. S1: **Weak antilocalization quantum conductance correction.** The sample presented in the main text exhibits a clear signature of the weak antilocalization effect in the low-temperature ($T = 50\,\mathrm{mK}$) magnetoconductance in the phase-coherent transport regime.

Singlet-Triplet Anticrossing in a Few-Electron Quantum Dot

The top gates can also be employed for an entirely different measurement setup. Although the top-gate width of 180 nm is relatively broad, two of the top gates can be used to create two tunnel barriers which enclose a quantum dot, a zero-dimensional charge island. The resulting charging energies are $E_c \simeq 6\,\mathrm{meV}$ and the excitation energies are in the order of $\Delta_{exc} = 2.5\,\mathrm{meV}$. We observe Coulomb blockade diamonds in the charge stability diagram and the width of the Coulomb diamonds in terms of plunger gate voltage changes with magnetic field. For odd (even) electron number parity the size of the diamonds is enhanced (reduced) with increasing magnetic field. Electron transport through the quantum dot can be described in terms of sequential tunneling of single charges. If an electron tunnels onto the quantum dot with an odd occupation, it can either occupy a singlet (total spin $S = 0$) or a triplet level (total spin $S = 1$). Owing to the different spin, the singlet and the triplet state experience a different energy shift in an external magnetic field. Hence, the two states can be brought to intersection, which occurs at $B = 3.0\,\mathrm{T}$ in Fig. S2. As a signature of spin-orbit coupling, the two states do not intersect but the degeneracy is lifted and an avoided crossing appears. This effect has previously been observed in single quantum dots formed in InAs nanowires[S8] and in InSb nanowires[S9]. The magnitude of the avoided crossing is given by $\Delta_{so} = 0.5\,\mathrm{meV}$. As an approximation, the avoided crossing can be related to the spin-orbit coupling strength via[S8]

$$\Delta_{so} = \frac{E_Z}{\sqrt{2}} \frac{r_e m^* \alpha_R}{\hbar^2}, \tag{S4}$$

with the Zeeman energy $E_Z = g\mu_B B$ and the effective electron distance r_e.

Measuring the Coulomb resonances as a function of the magnetic field yields the g factor of the quantum dot level. We find $g = 11$, which is larger compared to the g factors measured for the quantum point contact subbands[S1]. This indicates a Zeeman energy at the avoided level crossing of $E_Z = 1.9\,\mathrm{meV}$. It is well-known that the g factor is strongly diminished due to the orbital confinement[S10]. In our measurement geometry the lateral quantum dot confinement is weak and in the axial direction the quantum dot length is less than 180 nm[S11]. Our previous observation that the g factors in the quantum point contacts are significantly reduced compared to the bulk value of 14.7 indicates that the confinement strength in the quantum point contacts, which are formed right beneath the top gates, is much stronger than in the case of the quantum dots.

The effective electron distance can be estimated from the excitation energy, which reflects the overall confinement energy[S8]:

$$r_e \approx \sqrt{\hbar^2 / m^* \Delta_{exc}}. \tag{S5}$$

Thus, $r_e \approx 34\,\mathrm{nm}$ and $\alpha_R \approx 0.32\,\mathrm{eV\,Å}$. Hence, the spin-orbit energy can be estimated as $E_{so} = 170\,\mu\mathrm{eV}$. The Rashba parameter of the order of $\alpha_R \approx 0.3\,\mathrm{eV\,Å}$ is in good agreement with the value given above based on the weak antilocalization effect, which is a consistency check supporting the significance of Rashba spin-orbit coupling in our device. As discussed in the main text, the Rashba parameter in the quantum point contacts (QPCs) related to the reentrant conductance feature close to pinch-off is approximately a factor of four larger ($\alpha_R \approx 1.2\,\mathrm{eV\,Å}$). It is clear that the spin-orbit parameters are qualitatively different since the confinement configuration differs for all three cases. We expect that the confinement is very strong for the case of the QPC, where the constriction forms right under the gate electrode, whereas the quantum dot is formed between two gate electrodes and in the weak antilocalization measurement the top gates are grounded and the channel is in the weakly-confined multi-mode regime.

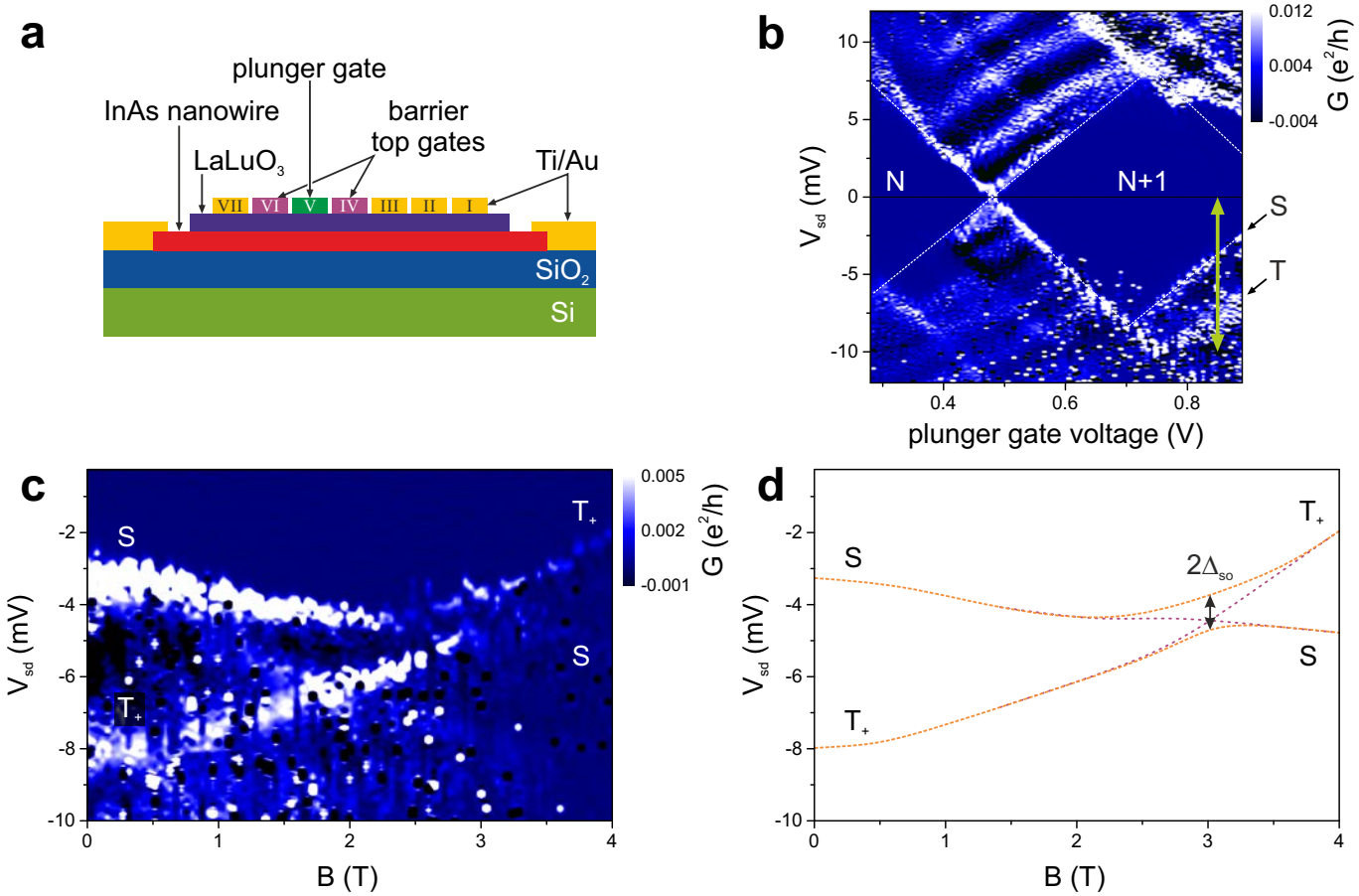

FIG. S2: **Sequential transport in a single quantum dot in the few-electron regime. a**, Cross-sectional schematic of the nanowire device. **b**, Conductance $dI/dV_{\rm sd}$ as a function of the source-drain voltage $V_{\rm sd}$ and the plunger gate voltage $V_{\rm TG-V}$. Top gate IV ($V_{\rm TG-IV} = -0.74\,{\rm V}$) and top gate VI ($V_{\rm TG-VI} = -0.76\,{\rm V}$) are used to create tunnel barriers in the nanowire that define the quantum dot in the device presented in the main text and top gate V works as a plunger gate which can shift the discrete energy levels of the quantum dot. Outside the Coulomb blockade diamonds the charge stability diagram features a number of lines related to excited states of the quantum dot. The green line indicates the source-drain voltage region which is scanned in (**c**). **c**, For an even number of electrons N the highest occupied states are singlets S and triplets $\rm T_{0,\pm}$. Spin-orbit interaction mixes S and $\rm T_+$, which gives rise to an avoided crossing when the states are brought to intersection at $B = 3.0\,{\rm T}$. **d**, Schematic representation of the avoided crossing between singlet and triplet levels in (**c**).

2. TWO-PARTICLE BACKSCATTERING-INDUCED HELICAL GAP

The Hamiltonian $H_{\rm soc}$ of a quantum wire with a single occupied confinement subband, in the presence of Rashba spin-orbit coupling and electron-electron interactions, can be conveniently expressed in terms of a Luttinger liquid with a charge and a spin degree of freedom[S12]. Explicitly, this reads

$$H_{\rm soc} = \frac{1}{2\pi}\int dx \sum_{\nu=\rho,\sigma} v_\nu K_\nu \left(\partial_x \theta_\nu\right)^2 + \frac{v_\nu}{K_\nu}\left(\partial_x \phi_\nu\right)^2 . \tag{S6}$$

Here, $K_\rho < 1$ ($K_\sigma > 1$), for repulsive interactions, is the Luttinger liquid parameter of the charge (spin) mode, v_ρ (v_σ) is the corresponding velocity, and θ_ν and ϕ_ν are canonically conjugated bosonic fields. The theory in equation (S6) is gapless. However, it is possible to introduce a gap at momentum $k = 0$ and for chemical potential $\mu = 0$ (see Fig. S3), by applying a magnetic field B perpendicular to the Rashba spin-orbit field. As can be seen in the fermionic picture, the process induced by the magnetic field is a hybridization of the bands at their crossing point by means of a standard Dirac mass term, as shown in Fig. S3a. In the bosonization language, the most relevant contribution to the Hamiltonian due to such a magnetic field reads

$$H_B = \frac{g\mu_B B}{2\pi a}\int dx \cos\left[\sqrt{2}\left(\phi_\rho + \theta_\sigma\right)\right], \tag{S7}$$

where g and μ_B denote the Landé g factor and the Bohr magneton, respectively, and a is the Luttinger liquid cut-off, which can be typically of the order of the inverse of the Fermi momentum[S13]. In our case, it is fixed to the spin-orbit wavelength $\hbar^2/m^*\alpha_{\rm R}$ by the condition $\mu = 0$. Similarly, correlated two-particle backscattering

$$H_{\rm 2p} = g_{\rm 2p}\int dx \cos\left[2\sqrt{2}\left(\phi_\rho + \theta_\sigma\right)\right], \tag{S8}$$

as pointed out in refs. 2 and 12 of the main text, can open a gap at $k = 0$ in the absence of external magnetic fields[S14,S15] ($g_{\rm 2p}$ is the coupling constant of two-particle backscattering, and has to be considered, at this stage, a free parameter). In that case, the process amounts to a correlated backscattering of two electrons instead of a single-particle backscattering, as in the case of the magnetic field. However, two ingredients are needed: in order for the contribution $H_{\rm 2p}$ to be relevant in the renormalization group sense, strong electron-electron interactions are essential, so to have $K_\rho + K_\sigma^{-1} < 1$, and axial spin symmetry must be broken. A first microscopic mechanism which can lead to the emergence of correlated two-particle backscattering has been pointed out in ref. 13 of the main text. There, the spin symmetry breaking term is provided by the coexistence of Rashba and Dresselhaus spin-orbit couplings. However, no sizeable Dresselhaus coupling is present in the system we inspect. A more promising microscopic mechanism responsible for the breaking of axial spin symmetry could be the coupling among two confinement subbands with different spin projections, which is induced by the Rashba spin-orbit interaction[S16], see Fig. S3b. In this context, two-particle backscattering emerges after a Schrieffer-Wolff transformation is performed, in order to integrate out the higher subbands and to obtain the effective Hamiltonian for the lowest confinement subband. The helical gap in the second subband should be much smaller than the one in the first subband for two reasons: On the one hand, the Landé g factor is smaller[S1] and hence, the single-particle effect is weaker. On the other hand, the interaction strength is weaker, most likely, because the particle density is larger. Therefore, we expect to observe the helical gap in the first subband but not in the second or in higher subbands.

A detailed description, which leads to the expression for the gap given in the main text once the identification $a \sim \hbar^2/m^*\alpha_{\rm R}$ is made, is provided in ref. S14. Explicitly, we have started the analysis with the Hamiltonian

$$H_w = H_0 + H_1 + V. \tag{S9}$$

Here,

$$H_0 = \sum_{n,k,s} \epsilon_{n,k,s} c^\dagger_{n,k,s} c_{n,k,s}, \tag{S10}$$

where $c_{n,k,s}$ is the fermionic operator for an electron in the subband $n = 0, \ldots, \infty$, with wave number k in the x direction and spin $s = \pm 1$. Further, $\epsilon_{n,k,s} = \frac{\hbar^2}{2m^*}(k + \frac{s m^* \alpha_{\rm R}}{\hbar^2})^2 + \hbar\omega n - \frac{m^*\alpha_{\rm R}^2}{2\hbar^2}$ is the single-particle energy term in conjunction with harmonic confinement (typical frequency ω) and the Rashba spin-orbit energy.

$$H_1 = -i\alpha_{\rm R} s\sqrt{\frac{m^*\hbar\omega}{2}}\sqrt{n+1}\left(c^\dagger_{n,k,s} c_{n+1,k,-s} - h.c.\right) \tag{S11}$$

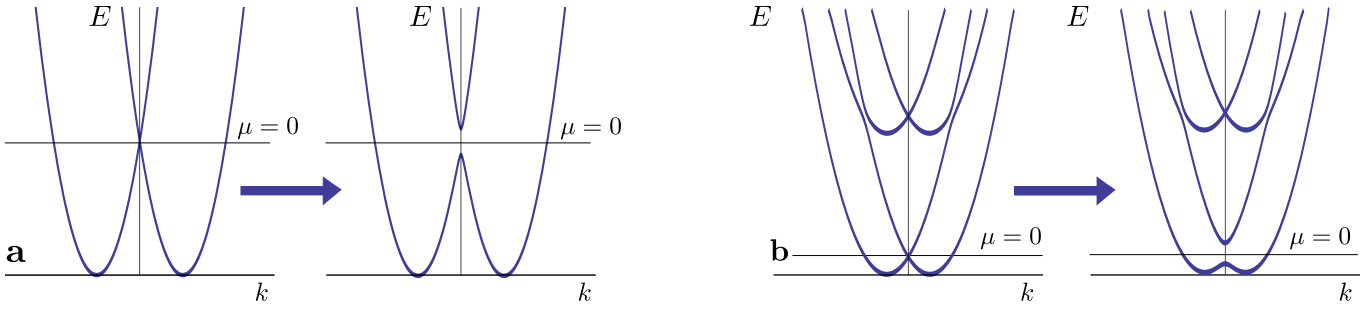

FIG. S3: **Different mechanisms responsible for helical gaps in Rashba quantum wires. a**, Schematic of the dispersion relation of the first subband of a spin-orbit coupled quantum wire, in case the coupling with higher subbands is neglected. A gap can be opened at the crossing point at $k = 0$ in the presence of a magnetic field applied perpendicular to the spin-orbit field. **b**, Schematic of the dispersion relation of the first two subbands of a spin-orbit coupled quantum wire. An avoided level crossing appears via the hybridization of subbands with different spin and different confinement quantum numbers due to Rashba spin-orbit coupling. Both two-particle backscattering due to Coulomb interactions and applied magnetic fields can open the helical gap at $k = 0$.

is the relevant subband coupling emerging from the spin-orbit interaction $-\alpha_R \sigma_x p_y$, where σ_x is the first Pauli matrix in the usual spin representation and p_y is the momentum in the confined direction. The electron-electron interaction V reads

$$V = \sum_{n_1,\ldots,n_4} \sum_{s,s'} \sum_{k,k',q} U_{n_1,n_2,n_3,n_4}(q)\, c^\dagger_{n_1,k+q,s} c^\dagger_{n_2,k'-q,s'} c_{n_3,k',s'} c_{n_4,k,s}, \tag{S12}$$

with

$$U_{n_1,n_2,n_3,n_4}(q) = \int \frac{dq_y}{2\pi} U(q,q_y)\, \Gamma_{n_1,n_2,n_3,n_4}(q_y), \tag{S13}$$

$$U(q,q_y) = \int dx dy e^{-i(qx+q_y y)} U(x,y), \tag{S14}$$

$$\Gamma_{n_1,n_2,n_3,n_4}(q_y) = \int dy_1 dy_2 e^{iq_y(y_1-y_2)} \phi^*_{n_1}(y_1)\, \phi^*_{n_2}(y_2)\, \phi_{n_3}(y_2)\, \phi_{n_4}(y_1),$$

where the functions ϕ are the eigenfunctions of the harmonic oscillator. The explicit expression we have adopted for electron-electron interaction is the screened Coulomb potential $U(x,y)$, given by

$$U(x,y) = \frac{1}{4\pi\varepsilon_0\varepsilon_r}\left(\frac{1}{\sqrt{x^2+y^2}} - \frac{1}{\sqrt{x^2+y^2+d^2}}\right), \tag{S15}$$

where ε_0 is the dielectric constant of the vacuum, ε_r is the dielectric constant relevant for the system, and d is the screening length. It can be shown that in order to integrate out the higher subbands, a suitable choice for the Schrieffer-Wolff operator S is

$$S = -\left[\sum_{n,k,s}\left(\frac{\sqrt{n+1}\alpha_R\sqrt{\frac{m^*\hbar\omega}{2}}}{\epsilon_{n,k,s}-\epsilon_{n+1,k,-s}} c^\dagger_{n+1,k,-s} c_{n,k,s}\right) - h.c.\right]. \tag{S16}$$

By applying the Schrieffer-Wolff transformation to V up to second order, two-particle backscattering terms naturally emerge[S14,S15]. Up to a numerical factor of order one, which depends on integrals over the wave functions, their amplitude is the result given in equation (1) of the main text.

Note that the effects of two-particle backscattering and of the applied perpendicular magnetic field are additive. We do not expect any gap closing while increasing the strength of the magnetic field, but rather a monotonic increase of the helical gap.

A comparison with other models of correlated one-dimensional systems is in order. The first issue is the relation to the 0.7 anomaly. The current understanding of the 0.7 anomaly, even in the presence of spin-orbit coupling, seems to be incompatible with the presence of reentrant features in the conductance profile in the absence of applied magnetic fields[S17,S18]. Moreover, features associated with the 0.7 anomaly have indeed been observed in the QPCs under

investigation, however in their conventional manifestation of shoulders in the conductance in the sub-open regime[S1]. The temperature dependence of the reentrant behaviour that we observe in the absence of applied magnetic fields is also incompatible with the phenomenology of the 0.7 anomaly: the expected enhancement of the feature with increasing temperature is in fact absent. From the theoretical perspective, on the other hand, our analysis is partially related to the idea of a density-dependent gap, which has been developed in the framework of the 0.7 anomaly[S19]. In that context, when the gap, as a function of the gate voltage, opens fast compared to the increase of the chemical potential, the model predicts the presence of a reentrant feature in the conductance at low temperature[S20]. However, within this model, even weak magnetic fields should cancel the feature. In fact, the Zeeman splitting of the bands would prevent the simultaneous crossing of the spin-up and spin-down band minima by the chemical potential, which would otherwise lead to a reentrant conductance behaviour. Hence, this model cannot properly explain the behaviour reported in the main text.

Another hallmark of strongly correlated one-dimensional systems is the formation of a Wigner molecule. The Wigner molecule is characterized by the very peculiar reduction of the linear conductance from $2e^2/h$ to e^2/h as the temperature overcomes the bandwidth of the spin excitations[S21]. We see no signature of this effect in any range of parameters we investigated, so that no Wigner molecule should be present in the system under investigation. A more careful analysis is needed in order to exclude the possibility of observing a zig-zag Wigner molecule[S22]. A first indication comes from the absence of a proper Wigner molecule at low densities, which should be the precursor of the zig-zag state. As a further indication, it needs to be mentioned that the reentrant features in the conductance that can be found in the zig-zag Wigner molecule are related to values between 0 and e^2/h and only present at high magnetic fields ($\sim 16\,\mathrm{T}$)[S23]. However, the conductance features we observe are located between e^2/h and $2e^2/h$ and are present even in the absence of applied magnetic fields, while magnetic fields overcoming the Rashba energy destroy the effect. Moreover, the physical mechanism causing the reentrant behaviour in the zig-zag state is related to a magnetic field-induced crossing in the energy levels[S23], which is not observed in the system inspected in this work (see Fig. 1c of the main text).

We hence believe that spin-orbit coupling, providing a crossing at $k = 0$ and hybridization with higher confinement subbands, offers the possibility for the opening of an interaction-induced gap for interactions that are not strong enough to drive the system in the Wigner molecule regime. This gives rise to a scenario which is very different from the conventional 0.7 anomaly in terms of temperature and magnetic field dependence.

3. REENTRANT CONDUCTANCE FEATURE

All nanowire quantum point contacts that have been investigated have shown a single reentrant feature on the first quantized conductance plateau at $G = 2e^2/h$ under certain conditions regarding the temperature, the dc-bias voltage and the back-gate voltage regime. At low temperatures and at small dc-bias voltages, it can be difficult to differentiate the feature from Fabry-Pérot resonances. However, the feature can also be masked due to bias-voltage or temperature averaging. Usually the reentrant conductance feature is enhanced by applying a positive back-gate voltage.

In short constrictions, the conductance in the gap regime is expected to rise due to electrons tunneling across the pseudogap region, rendering the reentrant conductance feature unrecognisable. The variation of the potential profile creating the QPC occurs on the characteristic length scale λ and plays an important role for the adiabaticity criterion[S24] $\lambda \sim \lambda^*$, which describes the optimal width of the gate potential profile $\lambda^* = \hbar v_F/(\Delta_{hel}/2)$. In order to fulfil this visibility condition, a certain ratio between Fermi velocity v_F and helical gap Δ_{hel} is required. With v_F extracted from the subband crossing at $k = 0$ ($v_F = \alpha_R/\hbar$) and $\Delta_{hel} = 1.1\,\text{meV}$, we find $\lambda^* = 218\,\text{nm}$. Hence, the actual smoothness of the electrostatic QPC potential of 60 nm that we can derive using a numerical Poisson-solver (cf. ref. S11) corresponds to the regime $\lambda \approx 0.3\lambda^*$, which, according to Rainis and Loss[S24], is close enough to the optimal adiabatic regime to ensure a good visibility of the reentrant region in the conductance.

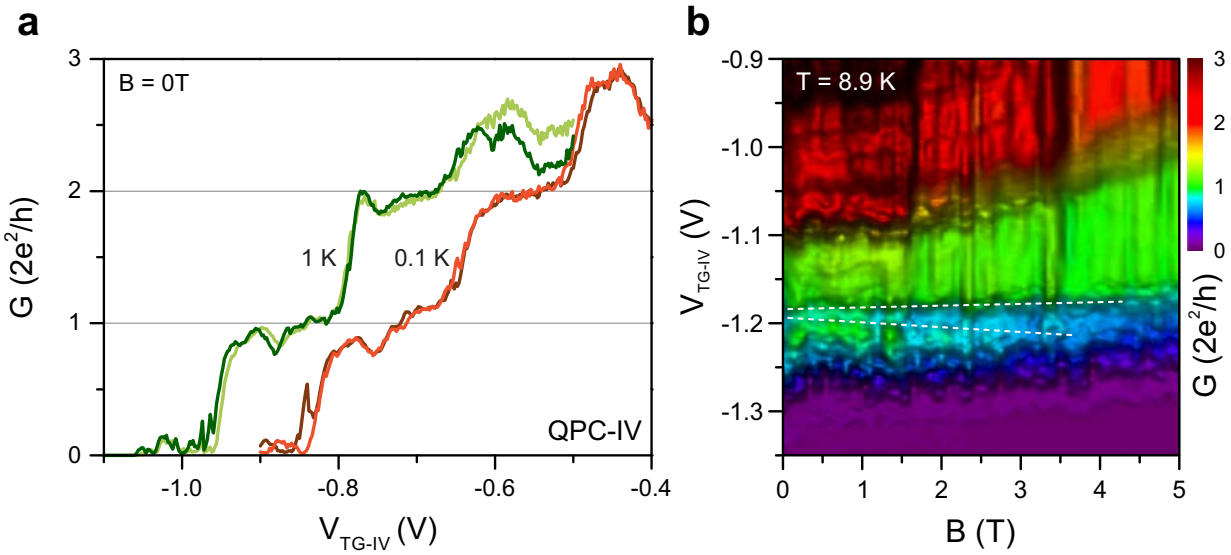

FIG. S4: **Temperature variation of the helical gap for QPC-IV. a**, Comparison of conductance curves for QPC-IV at 0.1 K (red and brown curves) and at 1 K (dark and light green curves). The dc-bias voltage for all curves was $V_{dc} = 4\,\text{mV}$ and no magnetic field has been applied. The green curves have been shifted by $-0.1\,\text{V}$ in top-gate voltage for clarity. The brown curve is identical to the zero-field trace from Fig. 1b of the main text and the red curve is identical to one of the traces presented in Fig. 2e of the main text. **b**, Conductance for QPC-IV at $T = 8.9\,\text{K}$ for different magnetic fields (same data as in Fig. 3b of the main text). The data was measured for zero dc-bias voltage, a transport regime which would be compromised by phase-coherent interference effects at lower temperatures (Fabry-Pérot resonances). The helical gap continuously evolves into the first Zeeman-split conductance plateau at $B > 4\,\text{T}$, where the conductance shoulder beneath the pseudogap feature has disappeared.

In Fig. S4a conductance curves for QPC-IV are compared for two different temperature values (0.1 K and 1 K) at the same dc-bias voltage of 4 mV. In both cases a clear reentrant behaviour can be observed on the first quantized conductance plateau while Δ_{hel} hardly changes with an average value of around 1.2 meV. At 8.9 K (see Fig. S4b) the gap at zero dc-bias voltage still amounts to approximately 1.1 meV, taking energy averaging at finite temperatures into account. Apart from this thermal averaging of the pseudogap feature no significant reduction of the gap can be observed. Since the proposed mechanism that opens the helical gap depends only on Coulomb interactions and Rashba SOC, no strong temperature dependence is anticipated. The conductance curves in Fig. S4 highlight the relatively weak effect of temperature and the robustness of the described helical gap feature.

Apart from QPC-II and QPC-IV presented in the main text, also data for QPC-I, III and V are presented below and they also exhibit the conductance characteristics related to a partial energy gap. All QPCs exhibit relatively similar gate lever arms of about $0.045 \pm 0.010\,\text{eV/V}$. Conductance curves showing a distinct dip feature for QPC-I and QPC-V are depicted in Fig. S5. The pseudogap feature for QPC-I (in Fig. S5a) resembles the one in the conductance trace

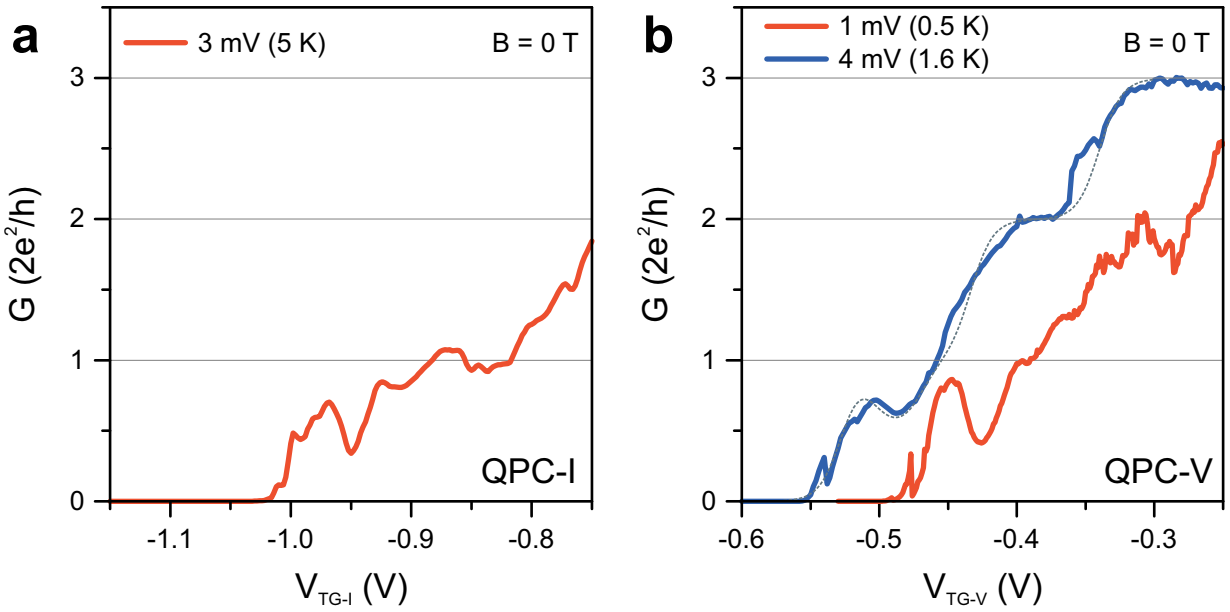

FIG. S5: **Signatures of the helical gap for different QPC devices. a**, The conductance at zero magnetic field measured for QPC-I at $T = 5\,\mathrm{K}$ and $V_{\mathrm{dc}} = 3\,\mathrm{mV}$ also exhibits a prominent reentrant behaviour on the $2\,e^2/h$-plateau compatible with a Rashba parameter of $\alpha_{\mathrm{R}} \approx 1.2\,\mathrm{eV\AA}$. **b**, Reentrant behaviour in the conductance of QPC-V at zero magnetic field for $T = 0.5\,\mathrm{K}$ and $V_{\mathrm{dc}} = 1\,\mathrm{mV}$ (red curve) and for $T = 1.6\,\mathrm{K}$ and $V_{\mathrm{dc}} = 4\,\mathrm{mV}$ (blue curve). Close to zero dc-bias voltage Fabry-Pérot resonances compromise the conductance quantization. In contrast to the other QPC devices, for QPC-V the transmission factor at $B = 0\,\mathrm{T}$ was reduced to around 0.5, which was compensated for in this plot. Also, the pinch-off voltage and the confinement energy is smaller for this QPC ($\hbar\omega_0 \sim 4\,\mathrm{meV}$). The grey dashed line shows the quantized conductance calculated for zero dc-bias, considering a helical gap of $\Delta_{\mathrm{hel}} = 1.5\,\mathrm{meV}$, a Rashba parameter of $\alpha_{\mathrm{R}} = 1.0\,\mathrm{eV\AA}$ and thermal averaging at $T = 4\,\mathrm{K}$. It is shifted together with the blue curve by $-0.05\,\mathrm{V}$ in top-gate voltage for clarity.

for QPC-IV at positive back-gate voltage ($V_{\mathrm{BG}} = 2\,\mathrm{V}$) in Fig. 4 of the main text. This can be attributed to variations in the pinch-off voltage and in the substantial confinement caused by the top gates that creates the QPCs and is responsible for the large SOC. The fact that for both curves the conductance feature is in agreement with a relatively large Rashba parameter corroborates this hypothesis. Here, we find $\alpha_{\mathrm{R}} \approx 1.2\,\mathrm{eV\AA}$ for QPC-I and $\alpha_{\mathrm{R}} \approx 1.3\,\mathrm{eV\AA}$ for QPC-IV at $V_{\mathrm{BG}} = 2\,\mathrm{V}$. In addition, also the spin-orbit gap is very similar for the two QPCs with $\Delta_{\mathrm{hel}} \approx 1.4\,\mathrm{meV}$, considering the Zeeman contribution to the helical gap in Fig. 4 of the main text.

For QPC-V, we find that the Rashba parameter is on the lower end of the parameter range (around $1.0\,\mathrm{eV\AA}$). However, the reentrant conductance feature is clearly visible (see Fig. S5b) and even dominates the first plateau. This is caused by the fact that the confinement energy (as well as the pinch-off voltage) is much smaller for this QPC. Here, $\hbar\omega_0$ is around 4 meV, which is expected to significantly enhance the two-particle backscattering mechanism. Already at a few Kelvin the conductance shoulder below the pseudogap region is smeared out due to thermal energy averaging (cf. blue curve). This can also be compared with the conductance trace calculated by assuming a helical gap of $\Delta_{\mathrm{hel}} = 1.5\,\mathrm{meV}$ (cf. dashed line in Fig. S5b).

In Fig. S6a another dataset is presented for QPC-III for different magnetic field values at zero dc-bias and at relatively high temperatures, thus enabling zero dc-bias measurements without superimposed Fabry-Pérot oscillations. The blue trace ($T = 10\,\mathrm{K}$) at $B = 0\,\mathrm{T}$ only exhibits a kink attributed to the 0.7 conductance anomaly[S1,S25] and at intermediate field values a reentrant conductance feature develops that broadens in agreement with the measured g factor of the lowest subband[S1] and eventually evolves into the Zeeman-split e^2/h-plateau. This QPC conductance regime is interesting from a fundamental point of view, as for example Goulko *et al.*[S18] have raised the question of how the 0.7 anomaly related to strong Coulomb interactions is affected by the presence of pronounced spin-orbit coupling. At 5 K also the zero-field reentrant conductance behaviour appears (see Fig. S6b) that we attribute to the interaction-induced helical gap. Applying a dc-bias voltage of $V_{\mathrm{dc}} = 2\,\mathrm{mV}$ causes the feature to disappear again (cf. blue curve in Fig. S6b). The observed features are in agreement with a Rashba parameter of $\alpha_{\mathrm{R}} \approx 1.1\,\mathrm{eV\AA}$.

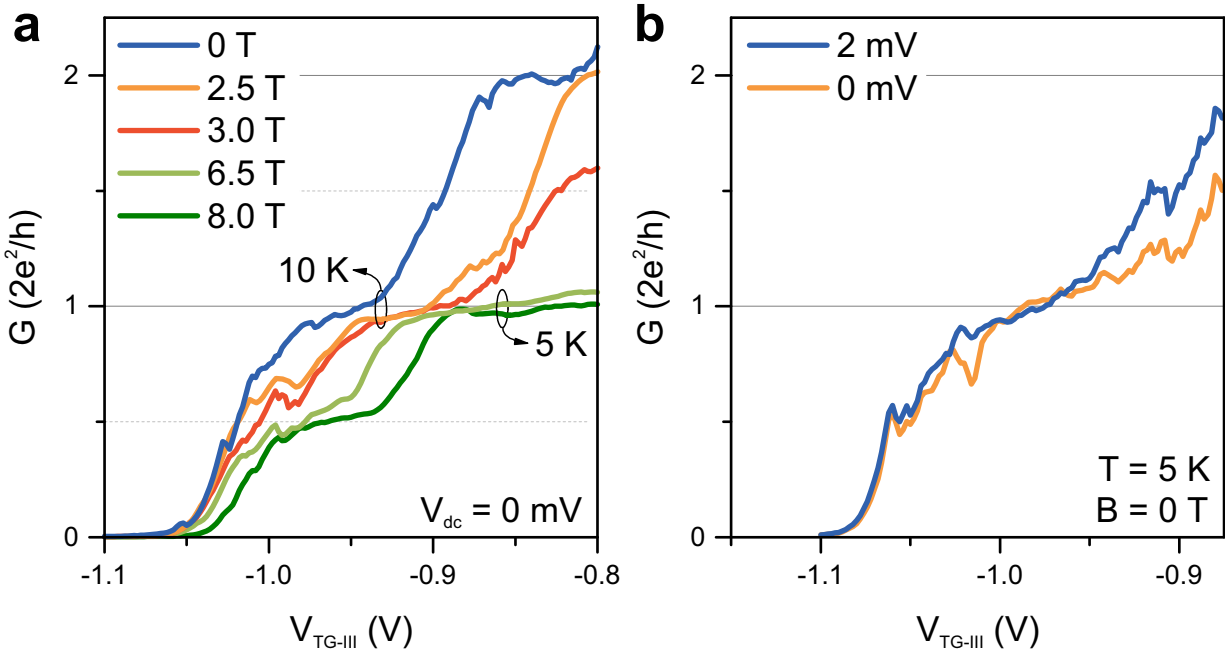

FIG. S6: **Reentrant conductance feature at higher temperatures for QPC-III. a**, Quantized conductance for QPC-III at $T = 10\,\mathrm{K}$ and at zero dc-bias voltage ($V_{\mathrm{ac}} = 80\,\mu\mathrm{V_{rms}}$). The dip feature on the first quantized conductance plateau appears at $B > 0\,\mathrm{T}$ and evolves into the first half-integer conductance step at e^2/h corresponding to the first non-degenerate spin-up subband. The high-field data (green traces) were taken at $T = 5\,\mathrm{K}$. **b**, At $T = 5\,\mathrm{K}$ the thermal energy averaging is small enough that the zero-field reentrant behaviour becomes visible ($B = 0\,\mathrm{T}$). Here, the blue curve corresponds to $V_{\mathrm{dc}} = 2\,\mathrm{mV}$ and the orange curve was measured for zero dc-bias voltage ($V_{\mathrm{ac}} = 80\,\mu\mathrm{V_{rms}}$). In (**b**) the dc-bias voltage was the sweep parameter and the two curves result from datapoints of successive differential conductance measurements at different values of $V_{\mathrm{TG-III}}$.

In Fig. S7 the impact of the back-gate voltage on the reentrant conductance feature is presented for QPC-II at $B = 1.5\,\mathrm{T}$, in analogy to Fig. 4 of the main text, where data are presented for QPC-IV. These traces exhibit a corresponding evolution of the conductance from a regime associated with a partial energy gap at positive back-gate voltages towards a double-plateau, which is related to conventional Zeeman splitting. This behaviour is in agreement with the interpretation that the back gate can not only tune the global Fermi level in the nanowire but also the local electric field responsible for Rashba spin-orbit coupling.

The spin-orbit energies for all QPCs are in the range of $E_{\mathrm{so}} = 1.7 - 2.9\,\mathrm{meV}$, corresponding to Rashba parameters of $\alpha_{\mathrm{R}} = 1.0 - 1.3\,\mathrm{eV\AA}$. The fact that all QPC devices exhibit very similar Rashba parameters shows that in spite of the small differences in the gate lever arm and the pinch-off voltage the variation in SOC parameters is not very pronounced among the QPCs. A variation of α_{R} of the order of $0.3\,\mathrm{eV\AA}$ is also what is required, in order to explain the appearance and disappearance of a single reentrant feature on the first quantized conductance plateau for the temperature and the magnetic field conditions presented in Fig. 4 of the main text and in Fig. S7. A significant tuning of the external Rashba parameter by more than $0.3\,\mathrm{eV\AA}$ has been demonstrated quantitatively in the diffusive, unconfined transport regime in a previous work (see ref. S4) for nearly identical dielectric surroundings. Due to thermal energy averaging and the magnetic field enhancement of the gap a comparable variation is sufficient, in order to drive the QPC channel from the helical transport regime into the fully spin-polarized Zeeman-dominated regime and vice versa.

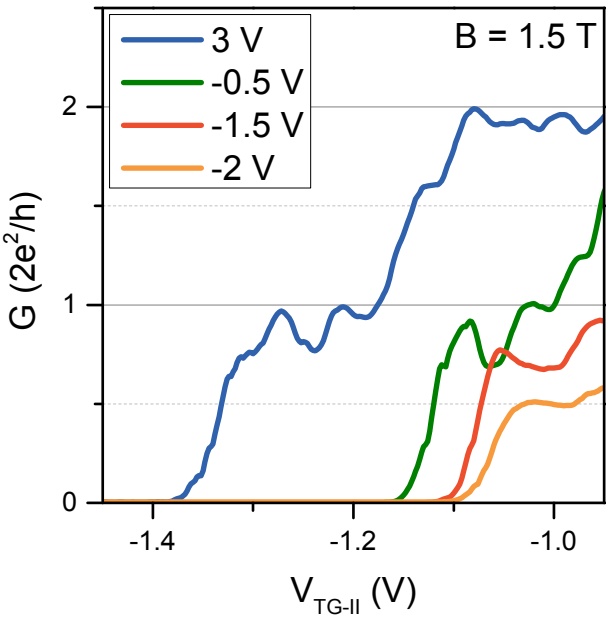

FIG. S7: **Impact of the back-gate voltage on the reentrant conductance feature for QPC-II.** Evolution of the reentrant conductance feature in the differential conductance for QPC-II as a function of back-gate voltage. The blue curve has been shifted by 0.1 V in top-gate voltage. All measurements are taken at a temperature of $T = 4\,\mathrm{K}$ and for a magnetic field of $B = 1.5\,\mathrm{T}$.

* Current address: QuTech, Delft University of Technology, 2628 CJ Delft, The Netherlands
† Electronic address: th.schaepers@fz-juelich.de

[S1] Heedt, S., Prost, W., Schubert, J., Grützmacher, D. & Schäpers, Th. Ballistic transport and exchange interaction in InAs nanowire quantum point contacts. *Nano Lett.* **16**, 3116–3123 (2016).
[S2] Hansen, A. E., Björk, M. T., Fasth, C., Thelander, C. & Samuelson, L. Spin relaxation in InAs nanowires studied by tunable weak antilocalization. *Phys. Rev. B* **71**, 205328 (2005).
[S3] Van Weperen, I. *et al.* Spin-orbit interaction in InSb nanowires. *Phys. Rev. B* **91**, 201413 (2015).
[S4] Kammermeier, M., Wenk, P., Schliemann, J., Heedt, S. & Schäpers, Th. Weak (anti)localization in tubular semiconductor nanowires with spin-orbit coupling. *Phys. Rev. B* **93**, 205306 (2016).
[S5] Beenakker, C. W. J. & van Houten, H. Boundary scattering and weak localization of electrons in a magnetic field. *Phys. Rev. B* **38**, 3232–3240 (1988).
[S6] Kurdak, Ç., Chang, A. M., Chin, A. & Chang, T. Y. Quantum interference effects and spin-orbit interaction in quasi-one-dimensional wires and rings. *Phys. Rev. B* **46**, 6846–6856 (1992).
[S7] Nitta, J., Bergsten, T., Kunihashi, Y. & Kohda, M. Electrical manipulation of spins in the Rashba two dimensional electron gas systems. *J. Appl. Phys.* **105** (2009).
[S8] Fasth, C., Fuhrer, A., Samuelson, L., Golovach, V. N. & Loss, D. Direct measurement of the spin-orbit interaction in a two-electron InAs nanowire quantum dot. *Phys. Rev. Lett.* **98**, 266801 (2007).
[S9] Nilsson, H. A. *et al.* Giant, level-dependent g factors in InSb nanowire quantum dots. *Nano Lett.* **9**, 3151–3156 (2009).
[S10] Kiselev, A. A., Ivchenko, E. L. & Rössler, U. Electron g factor in one- and zero-dimensional semiconductor nanostructures. *Phys. Rev. B* **58**, 16353–16359 (1998).
[S11] Heedt, S. *et al.* Adiabatic edge channel transport in a nanowire quantum point contact register. *Nano Lett.* **16**, 4569–4575 (2016).
[S12] Meng, T. & Loss, D. Strongly anisotropic spin response as a signature of the helical regime in Rashba nanowires. *Phys. Rev. B* **88**, 035437 (2013).
[S13] Gindikin, Y. & Sablikov, V. A. Deformed Wigner crystal in a one-dimensional quantum dot. *Phys. Rev. B* **76**, 045122 (2007).
[S14] Pedder, C. J., Meng, T., Tiwari, R. P. & Schmidt, T. L. $\mathbb{Z}_4$ parafermions & the 8π-periodic Josephson effect in interacting Rashba nanowires. *ArXiv e-prints* (2015). arXiv:1507.08881.
[S15] Pedder, C. J., Meng, T., Tiwari, R. P. & Schmidt, T. L. Dynamic response functions and helical gaps in interacting Rashba nanowires with and without magnetic fields. *Phys. Rev. B* **94**, 245414 (2016).
[S16] Governale, M. & Zülicke, U. Spin accumulation in quantum wires with strong Rashba spin-orbit coupling. *Phys. Rev. B* **66**, 073311 (2002).

[S17] Bauer, F. *et al.* Microscopic origin of the '0.7-anomaly' in quantum point contacts. *Nature* **501**, 73–78 (2013).
[S18] Goulko, O., Bauer, F., Heyder, J. & von Delft, J. Effect of spin-orbit interactions on the 0.7 anomaly in quantum point contacts. *Phys. Rev. Lett.* **113**, 266402 (2014).
[S19] Reilly, D. J. *et al.* Density-dependent spin polarization in ultra-low-disorder quantum wires. *Phys. Rev. Lett.* **89**, 246801 (2002).
[S20] Reilly, D. J. Phenomenological model for the 0.7 conductance feature in quantum wires. *Phys. Rev. B* **72**, 033309 (2005).
[S21] Matveev, K. A. Conductance of a quantum wire in the Wigner-crystal regime. *Phys. Rev. Lett.* **92**, 106801 (2004).
[S22] Meyer, J. S., Matveev, K. A. & Larkin, A. I. Transition from a one-dimensional to a quasi-one-dimensional state in interacting quantum wires. *Phys. Rev. Lett.* **98**, 126404 (2007).
[S23] Hew, W. K. *et al.* Incipient formation of an electron lattice in a weakly confined quantum wire. *Phys. Rev. Lett.* **102**, 056804 (2009).
[S24] Rainis, D. & Loss, D. Conductance behavior in nanowires with spin-orbit interaction: A numerical study. *Phys. Rev. B* **90**, 235415 (2014).
[S25] Micolich, A. P. What lurks below the last plateau: experimental studies of the $0.7 \times 2e^2/h$ conductance anomaly in one-dimensional systems. *J. Phys. Condens. Matter* **23**, 443201 (2011).